Journal of Materials Chemistry C

Unconventional superconductivity in 3*d* rocksalt transition metal carbides

Journal:	*Journal of Materials Chemistry C*
Manuscript ID	TC-ART-07-2019-003793.R1
Article Type:	Paper
Date Submitted by the Author:	31-Aug-2019
Complete List of Authors:	Szymanski, Nathan; University of Toledo College of Natural Sciences and Mathematics, Khatri, Indiras; University of Toledo Amar, Jacques; University of Toledo Gall, Daniel; Rensselaer Polytechnic Institute Khare, Sanjay V.; University of Toledo, Physics and Astronomy

Unconventional superconductivity in 3*d* rocksalt transition metal carbides

N. J. Szymanski[a], I. Khatri[a], J. G. Amar[a], D. Gall[b], S. V. Khare[a,*]

[a]Department of Physics and Astronomy, University of Toledo, Toledo, OH 43606, USA

[b]Department of Materials Science and Engineering, Rensselaer Polytechnic Institute, Troy, NY 12180, USA

*Corresponding Author: sanjay.khare@utoledo.edu

Abstract

Through calculation and analysis of electronic structure and lattice dynamics in 3*d* transition metal carbides, we identify MnC as a novel compound displaying unconventional superconductivity. Though unstable in the absence of applied pressure at 0 K, MnC may be stabilized above 300 K or 13 GPa due to enhanced t_{2g} orbital overlap or phonon-phonon interactions respectively. In the resulting structure, which adopts a ferromagnetic configuration with magnetization of 1.55 μ_B/Mn, we predict superconductivity occurring below a critical temperature of 16.2 K. Further investigation reveals this unconventional superconductivity derives from phonon-mediated minority-spin-triplet Cooper pairs, for which competing magnetic order is also suggested to play a role. Consideration of all 3*d* transition metal carbides yields a holistic explanation of trends in stability and superconductivity. Two unique cases are predicted: (i) FeC, with a critical temperature of 4.0 K, may be stabilized by temperature or pressure, whereas (ii) ZnC, with a high critical temperature of 27.8 K, remains stable at 0 K owing to complete filling and strong localization of its 3*d* shell. The findings here contribute to the understanding of factors influencing superconductivity, hence forming a basis on which a materials-by-design approach may be utilized for next-generation applications such as spintronic devices.

Significance Statement

We identify a new class of materials by predicting the coexistence of ferromagnetism and superconductivity in the rocksalt structure of MnC, for which stabilization is achieved above temperatures or pressures of 13 GPa or 300 K respectively. Further analysis reveals this type of superconductivity to derive from phonon-mediated pairing of minority-spin electrons, which is suggested to be assisted by competing magnetic interactions. In addition to MnC, a holistic study of all 3*d* transition metal carbides reveals two novel systems, FeC and ZnC, displaying conventional superconductivity below critical temperatures of 4.0 and 27.8 K respectively.

1 Introduction

Historically, transition metal carbides (TMCs) have been the subject of intense research interest owing to their exceptionally strong mechanical properties, which have led to the widespread utilization of various TMCs, such as TiC, in numerous industrial applications (1). Their unique properties, including high hardness and melting point, robust corrosion resistance, and good electrical conductivity, can be attributed to the delicate interplay between strong covalent and ionic bonding, as well as the presence of metallic *d*-*d* orbital interactions (2, 3). These features may be tuned by controlling the valence electron concentration (VEC) through choice of composition, therefore providing the opportunity to engineer novel materials with desired sets of properties (4-7). As a result of their open-framework electronic structure, TMCs have recently been realized as potential candidates for diverse applications related to energy storage (8), high-temperature superconductivity (SC) (9), and catalysis (10).

In this work, we focus on the emergence of SC in rocksalt 3*d* TMCs. The most well-studied TMCs adopting the rocksalt structure are group 4 carbides with a stoichiometric 1:1 metal-carbon ratio, e.g., TiC, ZrC, and HfC. These compounds are known to be thermodynamically stable owing to their VEC of 4, which allows complete occupation of bonding states while maintaining unfilled antibonding states (11, 12). In contrast, many other TMCs tend to crystallize in more complex stoichiometries and structures, e.g., $Cr_{23}C_6$ and Fe_3C, due to weakened metal-carbon bonding and large differences in ionic radii (13). However, previous works have demonstrated that certain group 5 and 6 TMCs, such as MoC, VC, and CrC, may be synthesized in the rocksalt structure remaining stable against decomposition under ambient conditions (14, 15). Several of these metastable TMCs have been shown to exhibit phonon-mediated SC, obeying the physics outlined by BCS theory (16), with critical temperatures (T_C) much higher than their group 6 counterparts. For example, previous experiments have revealed a T_C of 14 K for MoC (17) in comparison to a much smaller T_C of about 2 K for ZrC (18). Additionally, recent theoretical investigations have predicted even higher critical temperatures in the early-intermediate 3*d* TMCs VC and CrC, with T_C approximated at values near 25 K (9, 19, 20). It is typically agreed that the high-T_C SC occurring in these compounds is caused by increased electronic occupation at the Fermi level, which allows enhanced electron-phonon interactions to occur (17, 19, 20). Therefore, this suggests that further increases in T_C may be achieved in carbides of later transition metals, e.g., groups 7-12, through increased filling of higher-energy orbitals.

Study on late-group TMCs has been relatively limited owing to the difficulty of synthesizing stoichiometric compositions in crystalline form; instead, nanocrystalline or amorphous structures are adopted (13, 21). Analysis of electronic structure has concluded that the instability of late-group TMCs

in the rocksalt structure is caused by increased filling of antibonding orbitals, as well as decreased ionic character of the metal-carbon bonds (22). However, the detailed kinetic mechanism of destabilization based on features in the corresponding phonon dispersion curves remains unknown. Were these properties to be characterized and understood, it may become possible to remove the underlying sources of instability through controlled pressure (23), doping (24), or temperature (25). Similar methods have been implemented to influence the phase stability of various compositions in the rocksalt structure (26-29), but have not yet been extended to the case of TMCs.

Should stability of the intermediate-late 3*d* TMCs be attained, they would provide a model system to explore the correlations between VEC and properties giving rise to SC, e.g., electronic occupation at the Fermi level, electron-phonon coupling, and electron-electron interactions (16). Additionally, within the wide range of possible VEC values corresponding to the span of the 3*d* transition metals, ferromagnetic (FM) instabilities may be introduced should the Stoner criterion be satisfied, i.e., intra-atomic exchange and electronic occupation at the Fermi level become sufficiently strong such that FM ordering is preferred (30). Hence, there exists the potential for the rare case of coexisting long-range FM order and SC to occur within the rocksalt 3*d* TMCs. Such compounds have only recently been discovered (31) and the underlying physics is still not fully understood. It is generally agreed that these systems form Cooper pairs residing in a spin-triple state, as opposed to the usual singlet state of ordinary nonmagnetic superconductors, in order to withstand the strong FM background (32). However, there exists debate as to whether these Cooper pairs couple through phonons, as in standard BCS theory, or through magnons (33, 34). Finding unique new compounds displaying FM SC would provide further cases to study which may assist in solving this complex issue.

The aim of this work is to illustrate correlations between VEC, ionic/covalent bonding character, and SC through calculation and analysis of electronic structure and phonon dispersion curves. We confirm dynamic stability of the early TMCs (ScC, TiC, VC, and CrC) in the rocksalt structure at zero temperature and pressure. These findings also extend to ZnC, in which substantial *s*-*p* charge transfer and a filled 3*d* shell contribute to the overall stability. As for the intermediate-late TMCs, we find a boundary exists at the group 7-8 compounds MnC and FeC, for which an instability related to metal-metal dimerization is present at zero temperature and pressure. These TMCs become stable at pressures of 13 and 54 GPa respectively, or at temperatures above 100 K. The remaining TMCs, CoC, NiC, and CuC, are found to be completely unstable in the rocksalt structure, instead forming disordered configurations at non-zero temperatures. All stable compounds in this work are shown to be superconducting below their respective critical temperatures, with ZnC achieving the highest critical

temperature of 27.8 K due to strong electron-phonon coupling occurring throughout the full range of acoustic and optical frequencies. In MnC, we identify the potential coexistence of FM ordering and SC, for which the critical temperature may be tuned through application of pressure. Our findings provide insight into the underlying physics of unconventional SC by highlighting the importance of electron-phonon interactions in forming spin-triplet Cooper pairs, however, experimental investigation is necessary to confirm these results.

2 Computational Methods

All density functional theory (DFT) calculations have been performed using the Vienna Ab initio Simulation Package (VASP) (35-38). We have employed the Perdew-Burke-Ernzerhof (PBE) exchange correlation functional based on the generalized gradient approximation (GGA) within the framework of the projector augmented wave method (PAW) (39). A cutoff energy of 600 eV was used for the plane-wave basis set. In addition to the outer-core 4*s* and 3*d* electrons, semi-core 3*s* and 3*p* electrons were treated as valence states in Sc, Ti, and V, whereas semi-core 3*p* electrons were included for Cr and Mn. Only outer-core electrons were considered as valence states in Fe, Co, Ni, Cu, and Zn. All k-point meshes consisted of 6000 k-points per reciprocal atom (KPPRA). A convergence criterion of 10^{-6} eV with a Gaussian smearing value of width 0.1 eV was chosen for the electronic minimizations. Spin polarization was considered to account for magnetic ordering. FM, antiferromagnetic (AFM), and nonmagnetic configurations were tested for each compound. To investigate AFM ordering, we considered three configurations common to the rocksalt structure (40, 41): (i) moments alternating by layer in the [001] direction, (ii) moments alternating by layer in the [111] direction, and (iii) moments alternating every two layers in the [001] direction. Optimization of the corresponding magnetic moments was performed on 2×2×2 supercells. Only the lowest energy states were considered throughout the remaining calculations.

For the early TMCs ScC, TiC, VC, and CrC, initial structural configurations were taken from the Materials Project (42). In contrast, no structural parameters are available for the remaining compounds in this work; therefore, we assumed a starting volume equal to that of CrC. From these structures, geometric optimizations were performed by allowing the unit cell shape, volume, and ionic positions to relax until the force acting on each atom was less than or equal to 0.01 eV/Å. Zero-temperature dynamical stability of these compounds is investigated by studying their phonon dispersions curves within the framework of the harmonic approximation, assuming the independence of individual atomic vibrations (43). Hessian matrices were calculated for 5×5×5 supercells (of the 2-atom primitive cells) using density

functional perturbation theory (DFPT) (44). Utilizing these results along with the PHONOPY code (45), phonon frequencies were calculated along high-symmetry paths in the Brillouin zone.

Phonon dispersion curves were also studied as a function of pressure and temperature. The former is investigated by varying the volume below equilibrium and re-calculating the harmonic phonon dispersion curves for these compressed structures. For MnC and FeC, we have tested volumes ranging from 0% to 5% below the equilibrium value, in intervals of 1% (46). To determine the influence of thermal effects on the dynamical properties of compounds which are unstable at zero temperature and pressure, we have implemented the Temperature Dependent Effective Potential (TDEP) method, which accounts for anharmonic phonon-phonon interactions occurring at finite temperatures by constructing interatomic force-constant matrices using information obtained from molecular dynamics (MD) trajectories (47-49). Here, Born-Oppenheimer MD computations were conducted on 5×5×5 supercells using canonical NVT ensembles at temperatures of 100 K and 300 K, controlled by a Nosé thermostat (50). Simulations were carried out for 10,000 time steps of 1.5 fs each. From the results of these simulations, phonon dispersion curves were calculated with the TDEP package (47-49).

The electronic structure package QUANTUM-ESPRESSO (51, 52) was employed to study SC in all stable rocksalt 3*d* TMCs. For compounds requiring external pressure to become stable, i.e., FeC and MnC, unit cells of decreased volume corresponding to 13 and 54 GPa respectively were used throughout the SC computations allowing only real-valued phonon frequencies to be present. Kinetic effects of temperature are not explicitly included in the study of SC, i.e., molecular dynamics simulations are not used. However, dynamic properties in the form of phonon dispersions are considered. To this end, we used a dense 16×16×16 k-point grid along with a high plane-wave energy cutoff of 80 Ry to obtain dynamical matrices evaluated on a 16×16×16 q-point grid. From these matrices, full phonon spectra were calculated through Fourier transform. In accordance with previous works (53, 54), the Eliashberg function $\alpha^2F(\omega)$, which relates the contribution of each phonon frequency to the electron-phonon interaction, was computed using Allen's theory (55). By integrating this function across all frequencies, we found the electron-phonon interaction parameter λ, from which the superconducting critical temperature T_C was calculated using the modified McMillan formula (56, 57):

$$T_C = \frac{\omega_{ln}}{1.2}\exp\left[\frac{-1.04(1+\lambda)}{\lambda-\mu^*(1+0.62\lambda)}\right] \quad (1)$$

where ω_{ln} is the logarithmically averaged phonon frequency, considering all frequencies exhibiting non-zero phonon spectra, and μ^* is the Coulomb pseudopotential used to represent repulsive interaction

between electrons. Here, we have chosen μ^* according to the following relation which has been deemed suitable to describe electron-electron interactions in *d*-band metals (20, 58):

$$\mu^* = \frac{0.26N(E_F)}{1 + N(E_F)} \quad (2)$$

To account for suppression of phonon-mediated pairing in compounds exhibiting long-range magnetic order (MnC), we have used a modified equation developed and verified by Dolgov *et al*. (59):

$$T_C = \frac{\omega_{ln}}{1.45}\exp\left[\frac{-(1+\lambda_Z)}{\lambda_\Delta - \mu^*\left(1 + 0.5\frac{\lambda_\Delta}{1+\lambda_Z}\right)}\right] \quad (3)$$

For systems exhibiting spin-triplet SC, $\lambda_Z = \lambda_{ep} + \frac{1}{3}\lambda_{sf}$ and $\lambda_\Delta = \lambda_{ep} - \lambda_{sf}$ where λ_{ep} represents the regular electron-phonon interaction parameter and λ_{sf} represents coupling to spin fluctuations, given by:

$$\lambda_{sf} = \frac{3}{21} \frac{N(E_F)I^2}{- IN(E_F)} \quad (4)$$

where *I* is the Stoner parameter (30), chosen to be *I* = 0.3 in accordance with previous studies on similar Mn-based compounds (60, 61).

The formalism chosen here (Equations 2-4), while newly developed, has been demonstrated as a reliable technique when used to study systems displaying unconventional SC. Dolgov *et al.* illustrated that suppression of SC by spin-fluctuations causes a decrease in the critical temperature of $MgCNi_3$, which is not captured by the typical McMillan formula (Equation 1) (59). Without such corrections, the experimental value for T_C is significantly overestimated in compounds displaying long-range magnetic order along with SC. We note that the magnitude of this error does depend on the system; in compounds weakly influenced by spin-fluctuations, the improved agreement with experiment is minimal (e.g., < 1 K change in Mo_3Sb_7) (62), whereas the effects of spin-fluctuations become crucial in compounds with substantial magnetization (e.g., ~40 K change in FeB_4) (63). While the differences vary, improved accuracy is generally obtained in all cases using Equation (2).

3 Results and Discussion

3.1 Structural Stability

Calculated equilibrium lattice parameters of the TMCs are listed in Table 1, showing excellent agreement with the available experimental data (14, 15, 64, 65). A nearly parabolic relationship is observed between lattice constants and 3*d* occupations, i.e., group number. Moving from left to right across the early 3*d* TMCs (ScC, TiC, and VC), cell size decreases significantly. As displayed in Figure S1 (a) of the

Supplementary Material, these values show direct correlation with the metals' ionic radii owing to large differences between the metal/carbon electronegativities (66). For the intermediate TMCs (CrC, MnC, FeC, and CoC), changes in the lattice constant level off and only small deviations from linearity occur. In this case, Figure S1 (b) implies that the trend in cell size is more closely related to the metals' covalent radii (66), as high numbers of unpaired electrons in the group 6-9 transition metals mediate strong covalent bonding with carbon. In the late TMCs (NiC, CuC, and ZnC), substantial increases in the lattice constant are shown, being directly related to the metal's ionic radii. These compounds prefer to completely transfer their *s* electrons to carbon while maintaining their filled (or nearly filled) *d* shell.

Known ground states taken from the Materials Project (42) are geometrically and electronically relaxed into equilibrium using the aforementioned methods for consistent comparison of their energies. Such calculated energies of the rocksalt TMCs with respect to their binary metal-carbon convex hulls are listed in Table 1 along with energies of the FM configurations relative to the corresponding second-lowest energy state where applicable (MnC and CoC). Of the compounds tested, TiC is the only composition which is predicted to be thermodynamically stable in the rocksalt structure, whereas all other compositions lie above the convex hull and therefore may only be metastable. From an electronic perspective, TiC achieves stability due to its nominally d^0 configuration which provides four electrons to completely fill the carbon 3*p* shell. In contrast, Sc may only contribute 3 electrons to the partially filled 3*p* shell. As for most transition metals beyond group 4, excess electrons within the partially filled 3*d* shell fill antibonding orbitals, which will be discussed in greater detail throughout Section 3.2. ZnC presents a unique case which deviates from the trend of increasing energy resulting from complete filling of the 3*d* shell. However, as ZnC only contributes its two 4*s* electrons to the partially filled carbon 3*p* orbitals, it remains relatively energetically unfavorable and lies above the convex hull.

From calculation of phonon dispersion curves, we find that five compounds in this work are dynamically stable in the rocksalt structure at zero temperature and pressure. As shown in Figure 1, these compounds are ScC, TiC, VC, CrC, and ZnC as reflected by real-valued phonon frequencies throughout the Brillouin zone. Owing to the large differences between the masses of the transition metals and carbon, the acoustic modes in these systems are dominated by vibrations of metal atoms whereas optical modes are primarily attributed to vibrations of carbon atoms (67). As a result, the average magnitude of the acoustic frequency distribution is inversely related to the corresponding mass of the transition metal. In contrast, optical frequencies are most closely correlated with the lattice spacing (68); an inverse relation is illustrated between the average optical frequency and the lattice constant of the system. This causes the high-volume structures, such as ScC and ZnC, to exhibit low optical frequencies which overlap with

those of the acoustic modes, whereas low-volume structures, such as VC and CrC, display wide gaps between the acoustic and optical frequencies. Furthermore, between compounds exhibiting similar volume, covalent bond strengths influence the optical mode characteristics. Within the rocksalt structure, highly covalent/directional metal-anion bonds are known to be exceptionally resistant to deformations (69, 70). Hence, compounds containing strong covalent bonds (as will be discussed in Section 3.2) exhibit higher optical frequencies than those with weaker covalent character.

MnC and FeC represent interesting systems which are initially unstable as indicated by the presence of imaginary frequencies in the acoustic branches shown in Figure 2, but may be stabilized by means of temperature or pressure. To understand the origin of stabilization in these compounds, it is crucial to first characterize the source of instability. In both MnC and FeC, a common mode of imaginary character is observed in the doubly-degenerate transverse acoustic branches at the L point with $\vec{k} = \frac{2\pi}{a}(0.5, 0.5, 0.5)$. Further analysis reveals the eigenvector associated with this mode to cause increased overlap of second-nearest-neighbor metal-metal bonds. Accordingly, the interactions taking place during such distortions may be compared to the well-studied case of metal-metal dimerization occurring in many rutile oxides (71, 72). For both FeC/MnC and rutile oxides, increased filling of the *d* orbitals (to an extent) provides enhanced incentive for adjacent metal atoms to decrease their separation, therefore splitting the *d* t_{2g} states into bonding states, occupied by shared *d* electrons, and antibonding states lying above the Fermi level (72).

In rutile systems, d^1 compounds such as VO_2 may exist with or without metal dimers depending on temperature (71). Here, we identify both pressure and temperature as potential stabilizers of the rocksalt phase with equally spaced metal atoms. The former case is displayed in Figure 2; frequencies of the transverse acoustic branches shift upward as a function of pressure, becoming completely real-valued near pressures of 13 and 54 GPa for MnC and FeC respectively. Pressure-induced stabilization can be attributed to 1.64% and 4.01% decreases in Mn-Mn and Fe-Fe bond lengths respectively, causing increased overlap of the metal 3*d* t_{2g} orbitals. These changes allow enhanced bonding-antibonding splitting and therefore lower the overall energy of the system. Regarding differences between the two compounds, substantially higher pressure is needed to stabilize FeC due to its d^4 configuration, for which metal-metal bonding incentive is much greater than that of the d^3 configuration for MnC.

A separate mechanism of stabilization may take place due to thermal effects. As displayed in Figure 3 (a), upward shifts of the acoustic branches around the L point are observed as temperature is increased, with all frequencies becoming real-valued between 100 K and 300 K. Due to the computationally expensive nature of these calculations, we do not investigate further to more precisely

identify the critical temperature. In contrast to pressure, temperature provides stabilization through dynamical phonon-phonon interactions. Figure 3 (b) displays the energy landscape along the L mode eigenvector, which is characterized by Mn-Mn separation, for MnC at 0 K and 300 K. At 0 K, the overall energy of the system is decreased at small distortion magnitudes, in agreement with the imaginary frequency of the corresponding phonon dispersion curves. After a minimum energy is reached at Mn-Mn bond lengths of 2.605 Å, a steep upward trend in energy is observed owing to strong exchange interactions occurring at smaller bond lengths. As a result, the 0 K energy landscape forms a quartic double-well shape. However, as temperature and therefore the amplitudes of thermal vibrations increase, anharmonic interactions of adjacent Mn (or Fe) atoms become sufficiently strong to form an effective potential as shown in Figure 3 (b). The curvature of this effective potential is approximated using $\omega = \sqrt{k/m}$ where k represents the second derivative of energy with respect to position, m is the atomic mass of Mn, and ω is taken from the lowest calculated phonon dispersion branch at L. The upward concavity of the resulting potential, corresponding to a real-valued phonon frequency, implies dynamical stabilization of the rocksalt structure.

For all compounds in this work achieving stability, we identify the presence of numerous anomalies in the phonon dispersion curves. These features are characterized by significant deviations from the usual linearity or parabolicity of branches throughout local regions of the Brillouin zone. For example, Figure 1 shows that VC, CrC, MnC, FeC, and ZnC display a substantial dip along the longitudinal acoustic branch from Γ-X, i.e., in the direction of $\vec{k} = \frac{2\pi}{a}(0.5, 0.0, 0.5)$. Similar, though less pronounced, anomalies are also observed in branches near the K and L points, corresponding to $\vec{k} = \frac{2\pi}{a}(0.375, 0.375, 0.75)$ and $\frac{2\pi}{a}(0.5, 0.5, 0.5)$ respectively. As discussed in many previous works (73-76), these features are generally indicators of strong electron-phonon coupling. Hence, within the framework of BCS theory (16), our results imply the potential for phonon-mediated SC in the rocksalt 3*d* TMCs, given the electronic structure is metallic with sufficient density of states at the Fermi level.

Regarding the remaining compounds which have yet to be discussed (CoC, NiC, and CuC), we find that stability of the rocksalt structure may not be achieved at any reasonable temperature or pressure. As shown in Figure S2 of the Supplementary Material, the phonon dispersion curves of these compounds exhibit several branches of significant imaginary character throughout wide regions of the Brillouin zone, reflecting numerous instabilities. Our investigation reveals that these may not be overcome by pressure; no clear trend in the frequencies of the imaginary branches is observed as pressure is increased. With respect to temperature, reliable phonon dispersion curves are unable to be obtained as performing

molecular dynamics simulations for these systems leads to complete loss of long-range order. This phenomenon is exemplified by the radial distribution function (RDF) of NiC, displayed in Figure S3 of the Supplementary Material, in which the absence of any distinct bonding features beyond about 3 Å is demonstrated. Additionally, a new peak not present in the initial rocksalt structure is observed. This feature occurs near 1.4 Å and is associated with the formation of carbon-carbon bonds, which begin to congregate within the timescale of our calculations. Should longer timescales be tested, phase segregation into the elemental ground states of Ni and C may occur. Similar effects take place in CoC and CuC. The instability of these compositions in the rocksalt structure can be attributed to exceedingly weak metal-carbon bonds caused by low ionic and covalent character. As will be discussed in Section 3.2, the latter is caused by substantial filling of antibonding orbitals by the 3*d* electrons. Our findings here agree with previous works which have concluded that the late TMCs tend to adopt non-stoichiometric, disordered structures under ambient conditions (77, 78).

3.2 Electronic Structure and Bonding Characteristics

Electronic structure calculations reveal all compounds in this work to be metallic. This finding is reflected by the local density of states (LDOS) for each compound, displayed in Figure S4 of the Supplementary Material. To succinctly analyze the properties of these materials, we focus on four unique cases which span the 3*d* row: TiC, MnC, NiC, and ZnC. The projected density states (PDOS) and Crystal Orbital Hamiltonian Populations (COHP) of these compounds are displayed in Figure 4. As the ionic metal-carbon transfer of 4*s* electrons remains a constant factor throughout each compound, we exclude this point from the plots and discussion, instead focusing on covalent interactions. Owing to the octahedral ligand field surrounding each cation within the rocksalt structure, clear separation of the 3*d* t_{2g} and e_g orbitals occurs for nearly all compounds in this work. In TiC, which is representative of the early TMCs, carbon 2*p* states exhibit strong hybridization with Ti 3*d* t_{2g} states due to significant σ overlap, while weaker hybridization between 2*p* and 3*d* e_g states occurs due to π overlap. These features are supported by the COHP curves of TiC, showing a high degree of Ti-C bonding throughout energies from -6 eV to the Fermi level. We note that Ti-C antibonding emerges directly above the Fermi level; hence, the electronic occupation of TiC should provide the most energetically stable configuration (supported by Table 1). Decreasing valency, as in ScC, will lead to unfilled bonding orbitals whereas increasing valency, as in the intermediate-late TMCs, will cause antibonding orbitals to become partially filled. Regarding other bonding pairs (Ti-Ti and C-C), interactions remain relatively weak and do not contribute

significantly to the stability of the compound. The findings here agree well with previous works on TiC, which is well-studied for its strong bonding features and tough mechanical properties (4, 64, 69).

In MnC, for which the density of states is calculated at equilibrium (zero pressure) to highlight any instabilities, the low-energy electronic structure (-8 to -2 eV) is nearly identical to that of TiC, with slightly stronger bonding shown in this region of the COHP owing to enhanced covalent character of the Mn-C interaction. In contrast to the nominally d^0 configuration TiC, the increased valency of MnC leads to a d^3 configuration in which the remaining itinerant 3*d* electrons occupy the t_{2g} orbitals. As shown in the COHP, this leads to partial filling of the weakly-antibonding orbitals, which is likely a key factor in the energetic metastability of MnC. With respect to Mn-Mn interactions, a crucial feature arises near the Fermi level. Significant σ t_{2g}-t_{2g} overlap between second-nearest-neighbor metal atoms, as well as sufficient occupation of these orbitals in the d^3 configuration, leads to bonding-antibonding splitting with a region of relatively strong antibonding character lying halfway above and below the Fermi level. Therefore, a Stoner instability is introduced and it becomes energetically favorable for the electrons to rearrange into a FM configuration (30, 79). In optimizing the spin-polarized electronic structure, we report a 1.55 μ_B magnetic moment per Mn atom, as well as an induced -0.12 μ_B moment per C atom. The magnetic ordering here is reminiscent of similar compounds, MnP (80) and MnSi (81), in which Mn atoms align ferromagnetically at bond lengths comparable to those here (~2.86 Å). We also find an AFM configuration of comparable energy (~4.9 meV/f.u.), which will be discussed further in Section 3.4. All other ordering types tested here are unstable, leading to a non-magnetic configuration of significantly higher energy (~143 meV/f.u.), and are therefore not discussed further. As shown in Figure S4 of the Supplementary Material, the FM configuration of Mn moments allows the peak in majority-spin states to fall below the Fermi level while the corresponding peak in minority-spin states raise above it; hence, partial filling the antibonding states is avoided. While FM ordering may also be suspected in FeC, we find that it remains nonmagnetic as the Fermi level lies within a region of low electronic DOS, directly between two peaks, allowing the Stoner instability to be avoided. In contrast, CoC exhibits increased electron occupation and correspondingly a rise in the Fermi level which once again causes partial filling of metal-metal antibonding states, leading to the stabilization of a FM state with a moment of 0.20 μ_B/Co. All other compounds in this work remain nonmagnetic.

For NiC, which is representative of the unstable late TMCs, similar behavior to TiC and MnC is observed in the electronic structure at energies ranging from -9 to -3 eV. However, substantial occupation of strong metal-carbon antibonding orbitals, corresponding to σ e_g-*p* and π t_{2g}-*p* overlap, is found throughout energies ranging from -3 eV to the Fermi level. This energetically unfavorable exchange

interaction causes the metal-carbon bonds to become exceedingly weak within NiC and the other late TMCs of high valency. Such weak bonds, as well as significant carbon-carbon interactions which are amplified by the low volume of the structure, attribute to the instability of these compounds in the rocksalt structure. However, ZnC presents a unique case due to its completely filled *d* shell. As mentioned previously, Zn contributes its 4*s* electrons to the C *p* orbitals while maintaining its 3*d* electrons. These *d* states remain highly localized around -7 eV, with the t_{2g} and e_g orbitals being nearly degenerate owing to weak interactions with surrounding carbon atoms in the octahedral ligand field. As displayed in the COHP, ZnC displays nonbonding character throughout a wide range of energies, with the only peak in bonding interaction occurring near -7 eV. Although ZnC does achieve metastability due to the absence of occupied antibonding states, we conclude that the weak nature of the Zn-C bonds will likely cause the rocksalt structure to be susceptible to instability at room temperature.

3.3 Electron-Phonon Coupling and Conventional Superconductivity

The Eliashberg function $\alpha^2F(\omega)$ is plotted for all stable rocksalt 3*d* TMCs in Figure S5 of the Supplementary Material. Here, we choose to focus on the intermediate compound CrC as a model system to study the effects of electron-phonon interactions. Accordingly, the Eliashberg function and partial phonon density of states (PPDOS) of CrC are displayed in Figure 5 (a). The results show significant electron-phonon interactions in two major frequency ranges, 1-7 THz and 13-21 THz, directly coinciding with the acoustic and optical modes respectively. However, we find a large disparity between the contributions of each region, with $\alpha^2F(\omega)$ displaying substantially greater values throughout the acoustic frequencies. To highlight this, we have integrated $\alpha^2F(\omega)$ separately across acoustic and optical frequencies, obtaining electron-phonon interaction parameters of 2.291 and 0.788 for $\lambda_{acoustic}$ and $\lambda_{optical}$ respectively within CrC. As discussed in Section 3.1, the large differences between the masses of the metal and carbon atoms, e.g., 51.9961 and 12.0107 atomic mass units for Cr and C respectively (82), cause acoustic and optical modes to be dominated by vibrations of metal and carbon atoms respectively. Hence, the acoustic modes are mainly responsible for coupling to the metal 3*d* t_{2g} electrons existing near the Fermi surface, in agreement with previous works (19, 75, 83). This feature applies to TMCs consisting of partially filled *d* orbitals, whereas those with an empty (ScC and TiC) or completely filled (ZnC) *d* shell act differently, as will be demonstrated in later analysis of the Eliashberg function for ZnC.

Individual peaks in $\alpha^2F(\omega)$ are found to directly correlate with anomalies in the phonon dispersion curves. As shown in Figure 5 (a), CrC exhibits exceptionally strong coupling around two values in the acoustic frequencies: 3 THz and 5.2 THz. The former peak coincides with anomalies occurring in the

lower-frequency transverse acoustic branches near the high-symmetry X, K, and L points, whereas the latter peak coincides with anomalies occurring in the higher-frequency longitudinal acoustic branches near K and L (see Figure 1). The relative magnitudes of $\alpha^2F(\omega)$ in these two regions are directly related to the PPDOS in their respective range of frequencies. In contrast, although the PPDOS of CrC achieves higher values in the optical frequencies, $\alpha^2F(\omega)$ remains small owing to weak electron-phonon coupling, i.e., between metal *d* electrons and the carbon atoms. This property is reflected by the phonon dispersion curves, for which only minor anomalies occur, centered around frequencies of 17 THz and 19 THz, corresponding to modest peaks in $\alpha^2F(\omega)$.

To further elucidate the underlying causes of electron-phonon coupling, we have computed the Fermi surface of CrC. A two-dimensional slice cut orthogonal to the [101] direction and lying in the plane of the zone-center (Γ) is presented in Figure 5 (b), while the full surface is displayed in Figure S6 of the Supplementary Material. As discussed by Weber (75), phonon anomalies in rocksalt TMCs are associated with the topology of the Fermi surface, i.e., nesting of sheets in the directions along which anomalies in the phonon dispersion curves occur (83, 84). The complete surface of CrC is characterized by two large sheets (inner and outer), corresponding to bands crossing the Fermi level near X and K respectively, as well as small hole pockets occupying regions centered around K. Within the Γ-centered slice of the Fermi surface, we find that strong nesting is observed in two directions: (i) The slightly curved faces of the inner and outer sheets are parallel to one another, with a nesting vector ($\boldsymbol{q_1}$) in the direction of $\vec{k} = \frac{2\pi}{a}(0.375, 0.375, 0.75)$, i.e., the vector spanning Γ-K. (ii) The faces of the hole pockets are parallel to the edges of the inner sheet corners, with a nesting vector ($\boldsymbol{q_2}$) in the direction of $\vec{k} = \frac{2\pi}{a}(0.5, 0.0, 0.5)$, i.e., the vector spanning Γ-X. Indeed, these nesting features of the Fermi surface cause significant phonon anomalies, and therefore strong electron-phonon coupling, to occur throughout branches spanning Γ-X and Γ-K, in agreement with the observed features in our computed phonon dispersion curves. Additionally, the relative strengths of these anomalies can be attributed to the magnitudes of the nesting vectors $\boldsymbol{q_1}$ and $\boldsymbol{q_2}$, with the former being slightly larger than the latter.

As illustrated by Equation (1), the critical temperature of SC is dependent on three quantities: the electron-phonon interaction parameter (λ), the logarithmically averaged phonon frequency ($\omega_{\ln}$), and the electron-electron interaction parameter (μ^*). The corresponding computed values, along with the resulting critical temperature (T_C), are listed in Table 2. We find that all stable rocksalt 3*d* TMCs are capable of exhibiting SC at sufficiently low temperatures, with the magnitude of T_C varying significantly depending on the compound. In ScC, the highly ionic nature of the metal-carbon bonds leads to empty *d* orbitals which therefore limits coupling to acoustic modes. As a result, the electron-phonon interaction

parameter (λ = 0.524) and critical temperature (T_C = 3.0 K) of ScC remain low. An even lower critical temperature of 0.5 K is predicted for TiC owing to weak electron-phonon coupling (λ = 0.183) which results from low DOS at the Fermi level ($N(E_F)$ = 0.181). As discussed in Section 3.2, minimal DOS at the Fermi level is due to complete filling of the metal-carbon bonding orbitals in the nominally d^0 configuration of TiC. The addition of 3*d* electrons cause antibonding orbitals, for which the corresponding DOS displays a nearly constant positive slope at low energies, to become partially occupied. Hence, $N(E_F)$ and therefore λ increase linearly with respect to VEC for VC and CrC. Although CrC displays exceptionally strong electron-phonon coupling (λ = 3.079) due to a maximum in $N(E_F)$, its critical temperature is limited by a low logarithmically averaged frequency (ω_{ln} = 2.285 THz) and high degree of electron-electron interaction (μ^* = 0.180). Accordingly, VC and CrC exhibit nearly equal critical temperatures of 17.5 K and 17.4 K respectively.

As previous studies on the superconducting properties of TiC, VC, and CrC have been conducted, we may compare our findings with relevant data in the literature. For TiC, experimental works have reported critical temperatures ranging from 1.1 K to 1.8 K (18), which is reasonably close to the predicted value of 0.5 K in this work considering relative deviation in accuracy of the methods used (56, 57). In VC, experimentally reported values of 1.3 K to 1.8 K are much lower than our predicted value of 17.5 K, however, a highly non-stoichiometric phase ($VC_{0.82}$) was used in the corresponding experiments (18), indicating that defects strongly influence the superconducting characteristics of the system. The findings here also support recent theoretical works which found a relatively high T_C of ~11.5 K in stoichiometric VC (9, 67). As for CrC, no experimental work has been conducted to elucidate the possibility of superconductivity, however, theoretical works have predicted T_C values ranging from 24 K to 39 K (19, 20, 67), which are slightly higher than our calculated value of 17.4 K. Differences may be attributed to the choice of Coulomb pseudopotential (μ^*), as here we have chosen a variable choice of μ^* according to Equation (2) whereas other works have selected static values of approximately 0.1.

In MnC, for which the pressure-stabilized structure (13 GPa) is assumed, it may be expected that increased VEC leads to enhanced filling of antibonding orbitals and a higher DOS at the Fermi level. If a nonmagnetic state were assumed, this would be the case; however, as shown in Figure S4 of the Supplementary Material, the FM configuration of MnC causes peaks in the majority- and minority-spin states to shift below and above the Fermi level respectively. As a result, $N(E_F)$ is significantly decreased to 1.472, causing weakened electron-phonon coupling (λ = 1.494). Despite this effect, the increased ω_{ln} value of 4.491 THz, owing to upward shifts of dispersion curves in the compressed structure, allows MnC to achieve a relatively high critical temperature of 21.0 K. This value was determined within the

framework of conventional SC; however, further considerations of the FM background will be discussed in the next paragraph. Moving further down the 3*d* period to FeC, considered under an applied pressure of 54 GPa to maintain stability, increased VEC causes the first peak in the DOS of the antibonding states becomes completely filled, resulting in a Fermi level which lies directly between two peaks in the DOS. The low $N(E_F)$ of 0.574 leads to weak electron-phonon coupling ($\lambda = 0.548$) and therefore a low critical temperature of 4.0 K in FeC. As ZnC contains filled 3*d* orbitals, it does not follow the trend of the aforementioned TMCs. Here, the majority of *d* electrons remain highly localized at low energies whereas the partially filled *p* states span a wide range of energies and cross the Fermi level. Consequently, the *p* electrons existing near the Fermi surface are mainly responsible for conveying SC in ZnC, allowing optical phonons, deriving from vibrational modes of carbon atoms, to contribute significantly to electron-phonon interactions occurring in ZnC as indicated by the $\alpha^2F(\omega)$ function displayed in Figure S5 of the Supplementary Material. Hence, due to strong electron-phonon coupling throughout all phonon frequencies ($\lambda = 1.862$), as well as a relatively large ω_{ln} value of 4.232 THz and modest electron-electron interactions ($\mu^* = 0.1$), ZnC is predicted to exhibit a high critical temperature of 27.8 K. This finding confirms the previous prediction that T_C may be increased in rocksalt TMCs by enhancing electronic contributions from the light element, in this case C, at the Fermi level and therefore strengthening interactions with high-frequency optical phonons (85).

3.4 Unconventional Superconductivity: MnC

As discussed in Section 3.2, the ground state of MnC is predicted to be FM with a magnetic moment of 1.55 μ_B per Mn atom. We note this ordering remains energetically favorable throughout all pressures considered here. However, we also identify an AFM configuration, consisting of parallel Mn moments along common (100) sheets with antiferromagnetically coupling between adjacent sheets, which is only 4.9 meV/f.u. higher in energy than the FM configuration in the pressure-stabilized structure of MnC. This finding is reminiscent of the prototype FM superconductor UGe_2, for which SC arises on the border of itinerant ferromagnetism (31). Current theory suggests that such a delicate balance between FM and AFM coupling may be a crucial feature to produce spin-triplet SC in magnetic materials; competition between these interactions is thought to give rise to critical magnetic fluctuations mediating the formation of Cooper pairs in triplet states (31, 86). Though this mechanism may play a role in MnC, we propose electron-phonon interaction as an additional factor in allowing the existence of FM SC. Such a conclusion would agree with recent analysis of materials exhibiting both SC and Stoner magnetism (34).

As shown in Figure 6 (a), exchange splitting causes a significant downward shift in the energies of majority-spin bands in the compressed structure of MnC at 13 GPa, i.e., occupation of the majority-spin states is increased. Accordingly, the originally nested electronic bands lie far below the Fermi level, causing nesting to be almost completely absent from the corresponding majority-spin Fermi surface displayed in Figure 6 (b). In contrast, the minority-spin bands of MnC exhibit a slight upward shift in energy, i.e., occupation is decreased by a small amount. However, the overall structure of the minority-spin bands with respect to the Fermi level is maintained and therefore nesting is observed. This is reflected by the minority-spin Fermi surface of MnC displayed in Figure 6 (b), which is strikingly similar to that of CrC. Hence, our previous analysis holds and strong nesting is found along the X and K directions, leading to electron-phonon interactions, as described in Section 3.3, throughout these portions of the Brillouin zone. Interestingly, our findings imply that the minority-spin electrons are solely responsible for coupling to the phonons of MnC. Despite this unique limitation, electron-phonon coupling remains strong, which is a rare finding in materials exhibiting long-range FM order; some recent examples include strontium ruthenates (87) and doped manganites (88). Given the detrimental effects of internal magnetic fields on the formation of phonon-mediated Cooper pairs (32), FM ordering is likely to suppress the superconducting critical temperature. This correlation is supported by recent theoretical investigations in which the typical McMillan formula, Equation (1), greatly overestimates T_C due to suppression of SC by magnetic effects (59, 89). Therefore, 21.0 K represents an upper limit of T_C for MnC.

To obtain a more reliable prediction for the critical temperature of MnC, we use Equation (3) which has been shown to provide improved accuracy as applied to calculate T_C in systems exhibiting unconventional SC due to long-range magnetic order (59). Our calculations yield coupling to spin-fluctuations of the form $\lambda_{sf} = 0.524$, which serves to suppress phonon-mediated Cooper pairing, leading to a lowered critical temperature of 16.2 K. Additionally, as λ_A is found to be lower than μ^* (1.144 and 0.155 respectively), the phonon-mediated Cooper pairs in MnC must be of spin-triplet form (59), in agreement with most current theories on FM SC (32). More specifically, given that only minority-spin electrons interact strongly with the lattice, these pairs must be of the form $|\downarrow\downarrow\rangle$, unless magnon-mediated interactions are also determined to play a large role (31). Should our findings be confirmed by experiment, MnC would not only be the first Mn-based FM superconductor, but would also represent a high-T_C system in comparison to known U-based FM superconductors ($T_C < 1$ K) (90), instead showing T_C on the order of the recently discovered Eu-based FM superconductors in the "1411" structure type ($T_C \sim 35$ K) (91, 92). Furthermore, if the predicted T_C is found to be an overestimation and instead the formation

of Cooper pairs be completely suppressed by the magnetic background of MnC, we suggest the magnitude of the Mn moments may be decreased through application of pressure or doping (93, 94), hence increasing the probability for Cooper pairs to form and therefore allowing SC to arise.

4 Conclusion

In summary, we have studied the structural, thermodynamic, and electronic properties of all ten 3*d* TMCs in the rocksalt structure. The early TMCs (ScC, TiC, VC, and CrC) are found to be dynamically stable at zero temperature and pressure owing to complete occupation of metal-carbon bonding states and minimal filling of antibonding states. In contrast, instabilities related to metal-metal dimerization are introduced in the intermediate TMCs (MnC and FeC) due to significant *d*-*d* orbital overlap mediated by t_{2g} electrons of second-nearest-neighbor metal atoms. We find that these instabilities may be liberated through application of temperature or pressure, allowing increased orbital overlap and therefore stronger bonding-antibonding splitting. As for the late TMCs (CoC, NiC, and CuC), instabilities cannot be overcome by extrinsic conditions as a result of exceptionally weak metal-carbon bonds caused by substantial occupation of antibonding orbitals. However, due to its filled 3*d* orbitals which remain highly localized, ZnC maintains stability in the rocksalt structure; though, synthesis of this compound would likely present a challenge given its weak bond strengths and positive formation energy with respect to known binaries.

In the stable TMCs, analysis of Eliashberg functions $\alpha^2F(\omega)$ reveal strong electron-phonon interactions allowing SC to arise. For the majority of compounds, these interactions are mediated by coupling between 3*d* t_{2g} electrons existing near the Fermi surface and acoustic phonons associated with vibrational modes of the metal atoms. This is reflected by nesting in the Fermi surface, with corresponding nesting vectors showing direct correlation with phonon anomalies occurring near the high-symmetry points X and K in the Brillouin zone. In general, increased VEC causes greater occupation at the Fermi level, allowing stronger electron-phonon interaction and therefore a higher critical temperature, e.g., 17.4 K for CrC. However, MnC and FeC display lower critical temperatures as the Fermi level falls between states of significant antibonding character (due to FM exchange splitting in the former). ZnC, with a filled 3*d* shell, is a unique system in which *p* electrons are mainly responsible for conveying SC, causing coupling to both acoustic and optical modes and therefore a high critical temperature of 27.8 K.

In MnC, for which both FM ordering and SC is predicted, we utilize a modified description of spin-triplet Cooper pairs formed in the presence of a strong magnetic background. In doing so, we predict a critical temperature of 16.2 K. If confirmed by experiment, this finding would have significant

implications on the theory of unconventional SC: (i) The small energy difference between the FM and AFM configurations of MnC provides evidence supporting the theory that competing magnetic ordering is necessary to give rise to FM SC (32, 90). (ii) Our calculated values of λ_A and μ^* confirm that the Cooper pairs must be in triplet configurations (32) as opposed to the usual singlet states occurring in conventional superconductors (16). More specifically, these pairs are predicted to be of the form $|\downarrow\downarrow\rangle$ as the minority-spin electrons are responsible for coupling to the lattice. (iii) The phonon dispersion curves and Eliashberg functions imply that pairing may be mediated through electron-phonon interactions as in standard BCS theory (16) and recently suggested mechanisms of FM SC (34). Should MnC be successfully synthesized, it may have potential applications in spintronics designed to improve electronic circuit efficiencies (32). Considering the relative abundance of Mn in comparison to the active elements of most known FM superconductors, e.g. UGe_2 (31) and $CsEuFe_4As_4$ (92), MnC would also provide a cheaper and more sustainable material to be employed in SC-based spintronics devices.

Overall, this work provides insight into the direct correlations between VEC, covalent/ionic bonding strength, and phonon-mediated SC. The improved understanding of these connections may be utilized to engineer novel materials exhibiting desired properties, e.g., tuned superconducting critical temperature, through a materials-by-design approach by controlling structural features and VEC through implementation of alloying, doping, pressure, and/or temperature.

5 Acknowledgements

The computing for this project was performed at the Ohio Supercomputer Center (OSC) (95). We thank the National Science Foundation for funding this work through grants 1629230 and 1629239 under the CMMI. The authors also acknowledge funding support from the Air Force Research Laboratory, Space Vehicles Directorate, under Contract # FA9453-11-C-0253.

Table 1: Calculated (a_{calc}) and experimental (a_{exp}, where available) lattice parameters of the rocksalt structure, energy with respect to the corresponding metal-carbon convex hull (ΔE_{hull}) reported in the Materials Project (42), energy of the FM configuration (ΔE_{FM}) relative to the next lowest-energy state where applicable (AFM for MnC and non-magnetic for CoC), and characteristics of dynamical stability for each compound. Approximate necessary conditions of temperature or pressure for stabilization are also given. Each are considered separately, i.e., either the minimum value of temperature or pressure may be applied individually to achieve stability.

Compound	a_{calc} (Å)	a_{exp} (Å)	ΔE_{hull} (eV/f.u.)	ΔE_{FM} (meV/f.u.)	Dynamically Stable?
ScC	4.69	4.72[a]	0.696	-	Yes (0 K, 0 GPa)
TiC	4.33	4.33[b]	0.0	-	Yes (0 K, 0 GPa)
VC	4.16	4.18[c]	0.232	-	Yes (0 K, 0 GPa)
CrC	4.07	4.03[d]	0.670	-	Yes (0 K, 0 GPa)
MnC	4.05	-	0.956	-4.9	Yes (>100 K, 13 GPa)
FeC	3.99	-	1.406	-	Yes (>100 K, 54 GPa)
CoC	4.00	-	1.700	-5.2	No
NiC	4.07	-	2.612	-	No
CuC	4.23	-	3.786	-	No
ZnC	4.40	-	3.468	-	Yes (0 K, 0 GPa)

[a]: (65), [b]: (64), [c]: (15), [d]: (14)

Table 2: Calculated parameters influencing superconductivity in the stable rocksalt 3*d* TMCs. $N(E_F)$ represents the density of states (DOS) at the Fermi level, μ^* describes the electron-electron interaction parameter (dimensionless), ω_{ln} is the logarithmically averaged phonon frequency, λ corresponds to the electron-phonon interaction parameter (dimensionless), and T_C is the critical temperature below which superconductivity is predicted. For MnC, we provide values calculated with† and without consideration of the FM background. To account for the effective of net magnetization, modified electron-phonon interaction constants of $\lambda_A = 1.145$ and $\lambda_Z = 1.610$ are used.

Compound	$N(E_F)$ (states/eV)	μ^*	ω_{ln} (THz)	λ	T_C (K)
ScC	1.452	0.153	9.484	0.524	3.0
TiC	0.181	0.040	12.592	0.183	0.5
VC	0.980	0.129	3.228	1.645	17.5
CrC	2.262	0.180	2.285	3.079	17.4
MnC	1.472	0.155	4.491	1.494	21.0, 16.2†
FeC	0.574	0.095	4.549	0.548	4.0
ZnC	0.622	0.100	4.232	1.862	27.8

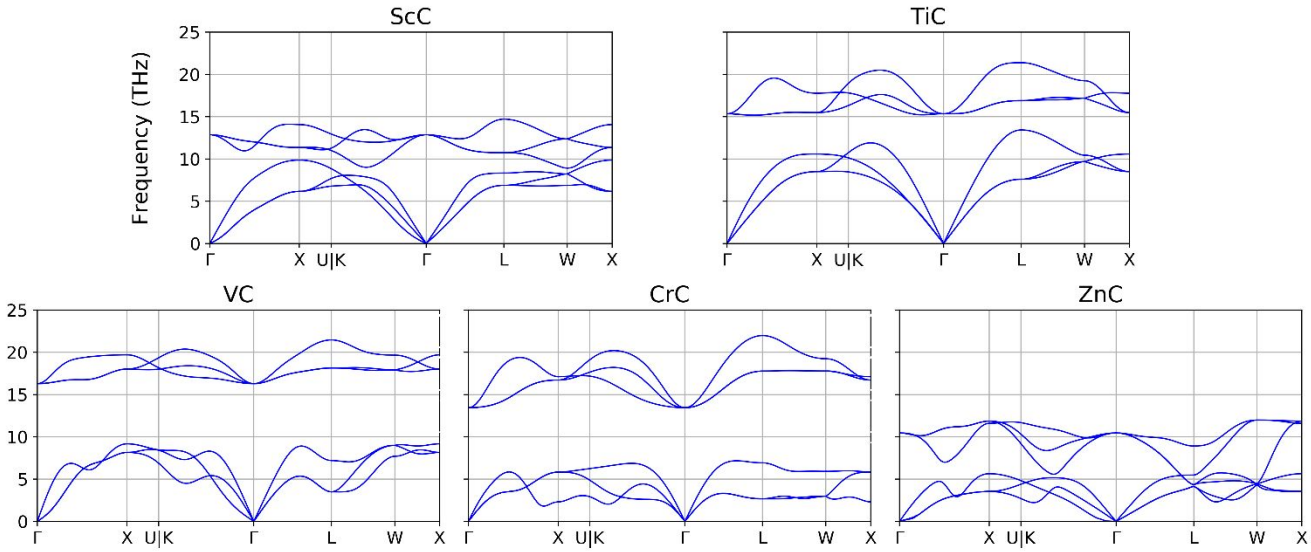

Figure 1: Phonon dispersion curves, calculated within the framework of the harmonic approximation, of the 3*d* TMCs which are found to be dynamically stable, i.e., no imaginary frequencies exist, at zero temperature and zero applied pressure.

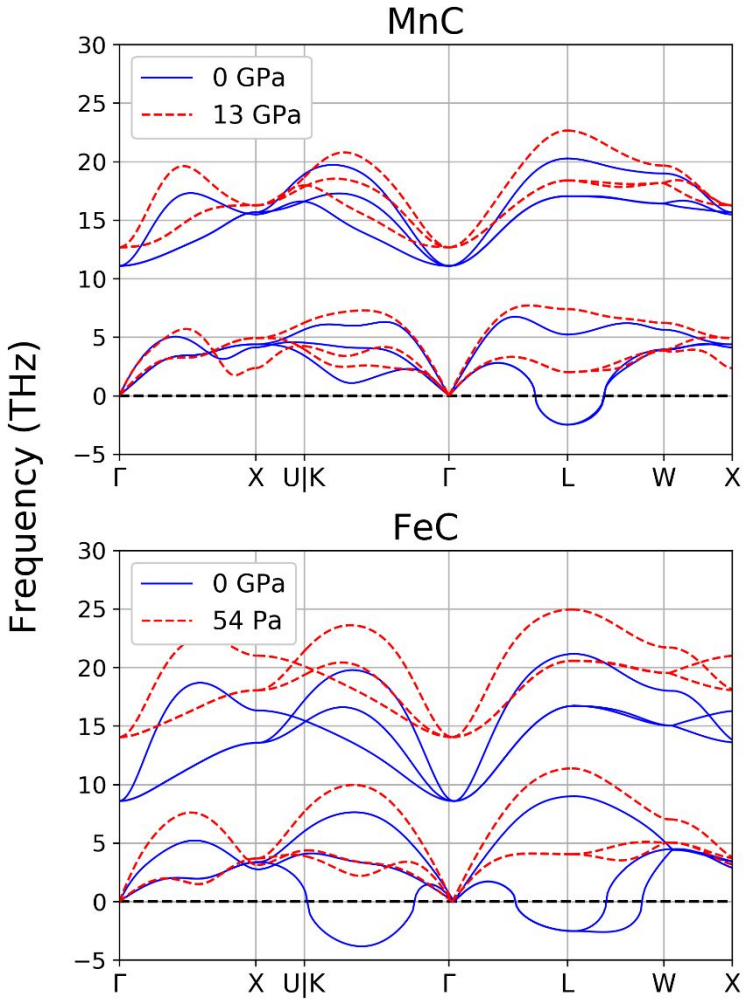

Figure 2: Phonon dispersion curves, calculated within the framework of the harmonic approximation, of MnC and FeC with and without applied external pressure. Positive values are real, whereas negative values corresponding to imaginary frequencies. For each compound, the pressure listed is nearly the minimum value needed for stabilization.

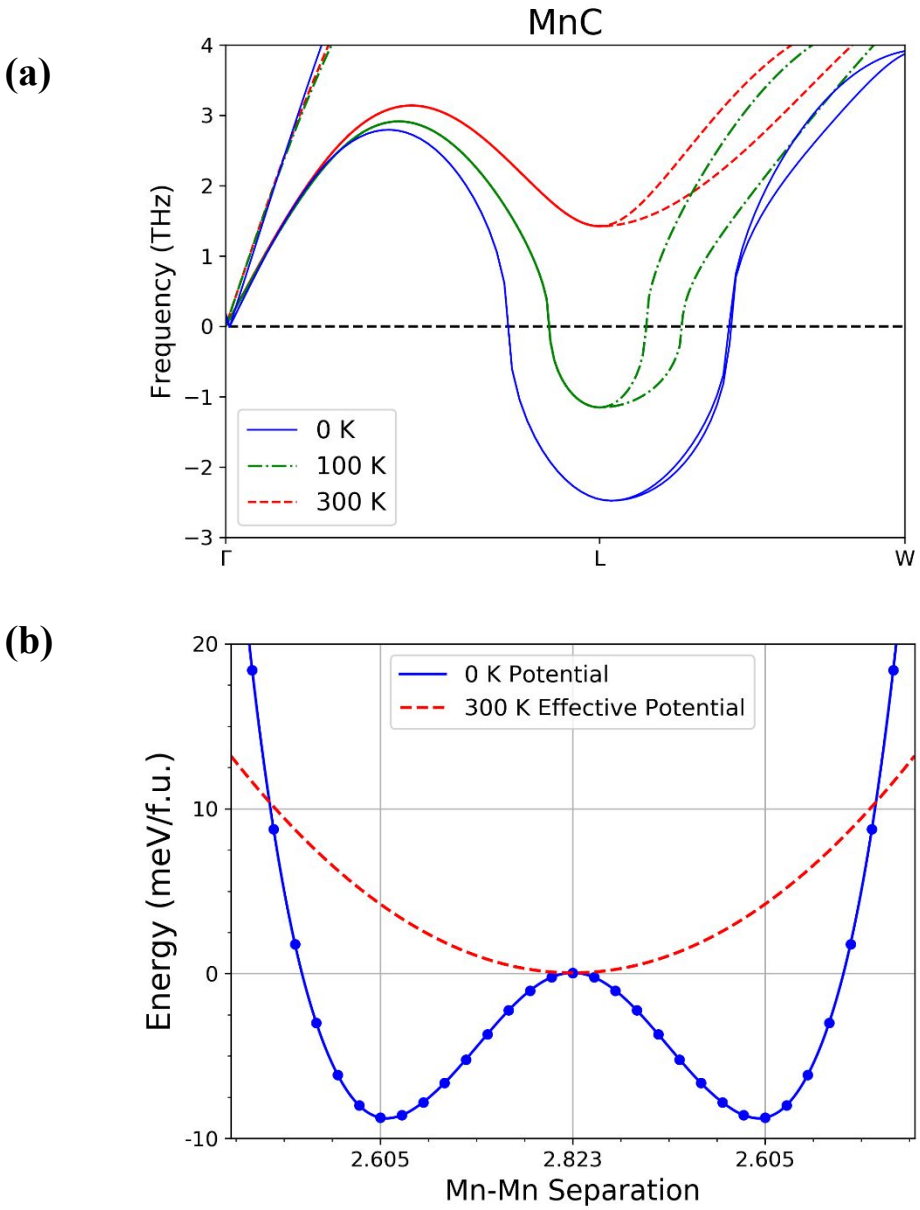

Figure 3: (a) Phonon dispersion curves, calculated within the framework of the Temperature Dependent Effective Potential (TDEP) method, of MnC at 0 K, 100 K, and 300 K. We focus on the L point, at which the features of the curves are highly sensitive to temperature. Positive values are real, whereas negative values corresponding to imaginary frequencies. (b) The energy landscape for MnC modulated by the L mode at 0 K and 300 K, showing dynamical stabilization resulting from anharmonic Mn-Mn interactions. Zero-temperature energies were calculated explicitly whereas finite-temperature energies are found by quadratic fitting based on the lowest phonon frequency occurring at L. Note that all corresponding calculations for (a) and (b) were performed at zero applied pressure.

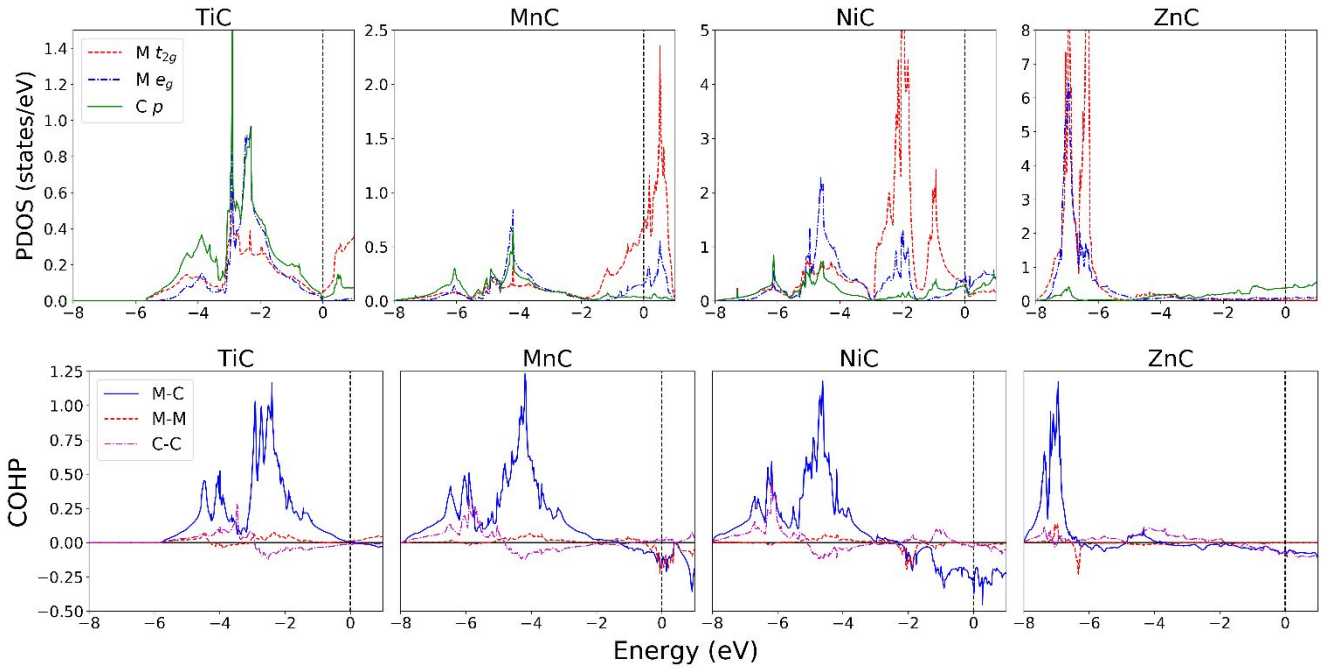

Figure 4: (Top) Projected density of states (PDOS) of four unique TMCs spanning the 3*d* row. Metal (M) 3*d* t_{2g} and e_g densities, as well as C *p* densities, are shown. The scales of y-axes vary to allow visualization of details. (Bottom) Crystal Orbital Hamiltonian Populations (COHP) of individual bonding pairs, metal-carbon (M-C), metal-metal (M-M), and carbon-carbon (C-C), are shown. Positive values represent bonding states, whereas negative values represent antibonding states. The scale of y-axes remains constant for all compounds. In both panels, the Fermi level is set to 0 eV. For MnC, a nonmagnetic configuration is used to illustrate the Stoner instability (30). The equilibrium structure (zero pressure) is assumed for each compound.

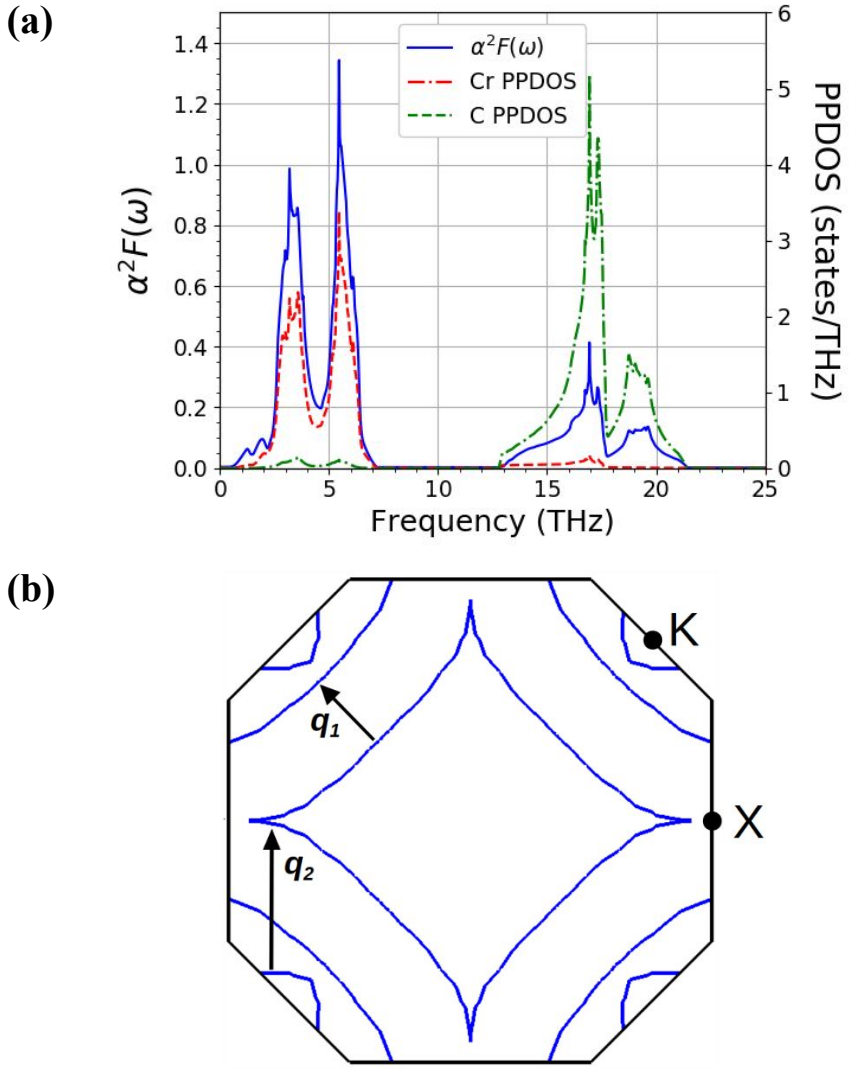

Figure 5: (a) The Eliashberg function $\alpha^2F(\omega)$, which relates the contribution of each phonon frequency to the electron-phonon interaction, is shown (left axis) along with the partial phonon density of states (PPDOS, right axis) of CrC, calculated within the framework of the harmonic approximation at zero applied pressure. (b) A two-dimensional slice of the Fermi surface of CrC, cut orthogonal to the [101] direction and lying in the plane of the zone-center (Γ). Nesting vectors are illustrated by $\boldsymbol{q_1}$ and $\boldsymbol{q_2}$, which are parallel to high-symmetry paths Γ-K and Γ-X respectively.

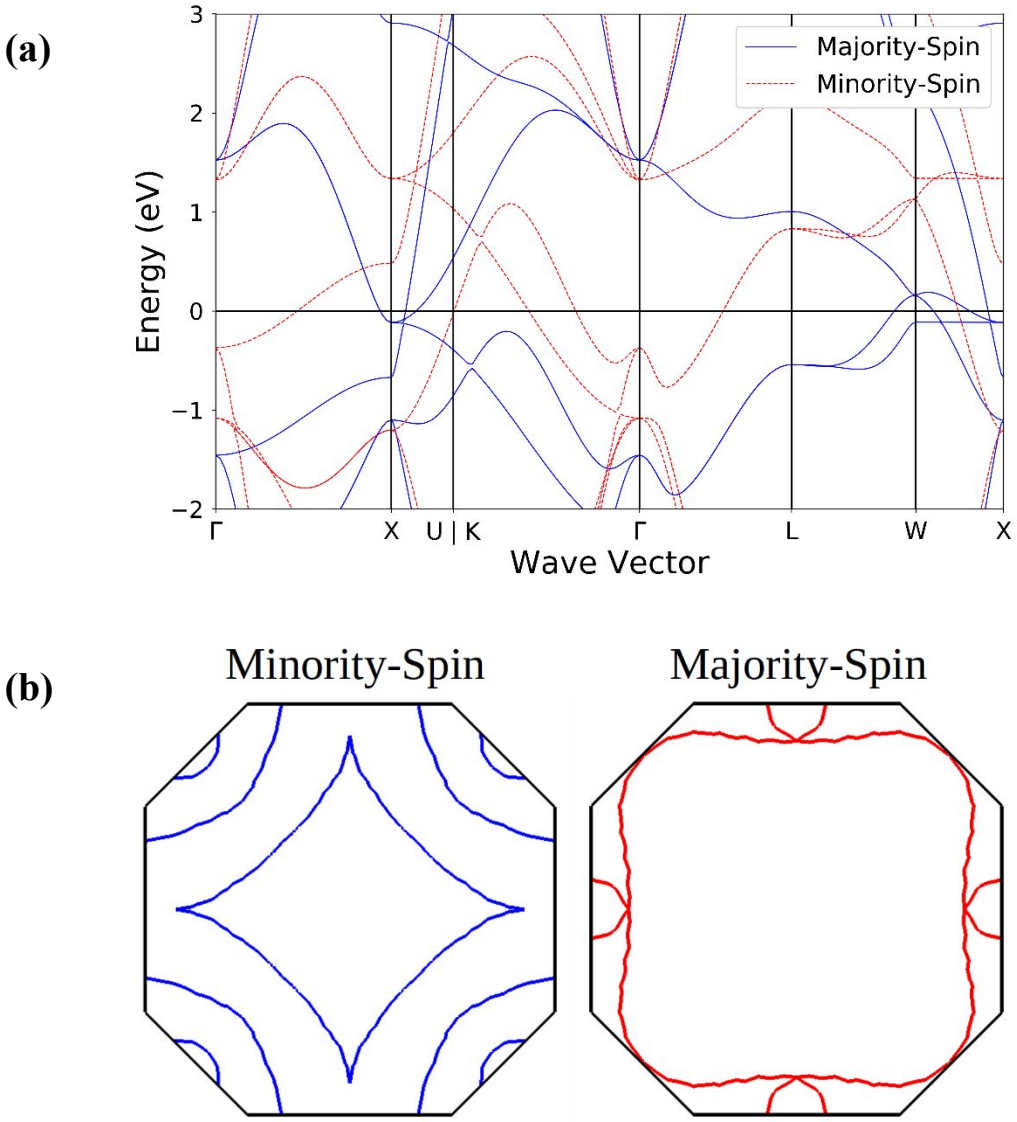

Figure 6: (a) The electronic band structure of MnC in the pressure-stabilized (at 13 GPa) ferromagnetic configuration, with the Fermi energy set to 0 eV. (b) Two-dimensional slices of the Fermi surface of MnC, cut orthogonal to the [101] direction and lying in the plane of the zone-center (Γ). Separate plots are shown for the minority- and majority-spin surfaces.

References

1. H. H. Hwu, J. G. Chen, Surface chemistry of transition metal carbides. *Chem. Rev.* **105**, 185 (2005).
2. H. Li *et al.*, Structural, elastic and electronic properties of transition metal carbides TMC (TM= Ti, Zr, Hf and Ta) from first-principles calculations. *Solid State Commun.* **151**, 602 (2011).
3. J. A. Warner, S. K. R. Patil, S. V. Khare, K. C. Masiulaniec, Ab initio calculations for properties of MAX phases Ti_2TlC, Zr_2TlC, and Hf_2TlC. *Appl. Phys. Lett.* **88**, 101911 (2006).
4. K. Balasubramanian, S. V. Khare, D. Gall, Valence electron concentration as an indicator for mechanical properties in rocksalt structure nitrides, carbides and carbonitrides. *Acta Materiala* **152**, 175 (2018).
5. D.-B. Kang, Effect of Valence Electron Concentration on Elastic Properties of 4d Transition Metal Carbides MC (M = Y, Zr, Nb, and Rh). *Bull. Korean Chem. Soc.* **34**, 2171 (2013).
6. Z. T. Y. Liu, X. Zhou, S. V. Khare, D. Gall, Structural, mechanical and electronic properties of 3d transition metal nitrides in cubic zincblende, rocksalt and cesium chloride structures: a first-principles investigation. *J. Phys.: Condens. Matter* **26**, 025404 (2014).
7. X. Zhou, D. Gall, S. V. Khare, Mechanical properties and electronic structure of anti-ReO_3 structured cubic nitrides, M_3N, of d block transition metals M: an ab initio study *J. Alloy. Compd.* **595**, 80 (2014).
8. Y. Zhong *et al.*, Transition Metal Carbides and Nitrides in Energy Storage and Conversion. *Adv. Sci.* **3**, 1500286 (2016).
9. R. Zhan, X. Luo, Topologically nontrivial phases in superconducting transition metal carbides. *J. Appl. Phys.* **125**, 053903 (2019).
10. M. Nagai, T. Kurakmai, Reverse Water Gas Shift Reaction over Molybdenum Carbide. *J. Chem. Eng. Jpn.* **38**, 807 (2005).
11. J. Häglund, A. F. Guillermet, G. Grimvall, M. Körling, Theory of bonding in transition-metal carbides and nitrides. *Phys. Rev. B* **48**, 11685 (1993).
12. Z. T. Y. Liu, D. Gall, S. V. Khare, Electronic and bonding analysis of hardness in pyrite-type transition metal pernitrides. *Phys. Rev. B* **90**, 134102 (2014).
13. U. Jansson, E. Lewin, Sputter deposition of transition-metal carbide films — A critical review from a chemical perspective. *Thin Solid Films* **536**, 1 (2013).
14. B. X. Liu, X. Y. Cheng, A metastable Cr carbide of NaCl structure formed by carbon-ion implantation into chromium films. *J. Phys.: Condens. Matter* **4**, L265 (1992).
15. R. W. G. Wyckoff, *Crystal Structures* (John Wiley & Sons, 1963).
16. J. Bardeen, L. N. Cooper, J. R. Schrieffer, Theory of Superconductivity. *Phys. Rev.* **108**, 1175 (1957).
17. R. H. Willens, E. Buehler, B. T. Matthias, Superconductivity of the Transition-Metal Carbides. *Phys. Rev. B* **159**, 327 (1967).
18. W. T. Ziegler, R. A. Young, Studies of Compounds for Superconductivity. *Phys. Rev.* **90**, 115 (1953).
19. H. M. Tütüncü, S. Bağci, G. P. Srivastava, A. Akbulut, Electrons, phonons and superconductivity in rocksalt and tungsten–carbide phases of CrC. *J. Phys.: Condens. Matter* **24**, 455704 (2012).
20. M. Kavitha, G. S. Priyanga, R. Rajeswarapalanichamy, K. Iyakutti, Structural stability, electronic, mechanical and superconducting properties of CrC and MoC. *Mater. Chem. Phys.* **169**, 71 (2016).
21. K. Schwarz, Band structure and chemical bonding in transition metal carbides and nitrides. *Crit. Rev. Solid State Mater. Sci.* **13**, 211 (1987).

22. Q. Wang *et al.*, Explaining stability of transition metal carbides – and why TcC does not exist. *RSC Adv.* **6**, 16197 (2016).
23. X. Zhou, J. L. Roehl, C. Lind, S. V. Khare, Study of B1 (NaCl-type) to B2 (CsCl-type) pressure-induced structural phase transition in BaS, BaSe and BaTe using ab initio computations. *J. Phys.: Condens. Matter* **25**, 075401 (2013).
24. Z. T. Y. Liu, B. P. Burton, S. V. Khare, D. Gall, First-principles phase diagram calculations for the rocksalt-structure quasibinary systems TiN-ZrN, TiN-HfN and ZrN-HfN *J. Phys.: Condens. Matter* **29**, 035401 (2017).
25. N. J. Szymanski, L. N. Walters, O. Hellman, D. Gall, S. V. Khare, Dynamical Stabilization in Delafossite Nitrides for Solar Energy Conversion. *J. Mat. Chem. A* **6**, 20852 (2018).
26. P. Bhardwaj, S. Singh, Pressure induced structural phase transitions—A review. *Cent. Eur. J. Chem.* **10**, 1391 (2012).
27. M. Pandey, R. G. S. Pala, Stabilization of Rocksalt CdSe at Atmospheric Pressures via Pseudomorphic Growth. *J. Phys. Chem. C* **117**, 7643 (2013).
28. A. Zaoui, M. Ferhat, Pressure-induced changes in electronic and vibrational properties of LaS. *Phil. Mag. Lett.* **93**, 152 (2013).
29. K. Balasubramanian, S. V. Khare, D. Gall, Vacancy-induced mechanical stabilization of cubic tungsten nitride. *Phys. Rev. B* **94**, 174111 (2016).
30. S. Blundell, *Magnetism in Condesned Matter* (Oxford University Press, USA, 2001).
31. S. S. Saxena *et al.*, Superconductivity on the border of itinerant-electron ferromagnetism in UGe2. *Nature* **406**, 587 (2000).
32. J. Linder, J. W. A. Robinson, Superconducting Spintronics. *Nat. Phys.* **11**, 307 (2015).
33. R. Kar, T. Goswami, B. C. Paul, A. Misra, On magnon mediated Cooper pair formation in ferromagnetic superconductors. *AIP Adv.* **4**, 087126 (2014).
34. R. Ojajärvi, T. Hyart, M. A. Silaev, T. T. Heikkilä, Competition of electron-phonon mediated superconductivity and Stoner magnetism on a flat band. *Phys. Rev. B* **98**, 054515 (2018).
35. G. Kresse, J. Furthmüller, Efficiency of ab-initio total energy calculations for metals and semiconductors using a plane-wave basis set. *Comput. Mat. Sci.* **6**, 15 (1996).
36. G. Kresse, J. Furthmüller, Efficient iterative schemes for ab initio total-energy calculations using a plane-wave basis set. *Phys. Rev. B* **54**, 11169 (1996).
37. G. Kresse, J. Hafner, Ab initio molecular dynamics for liquid metals. *Phys. Rev. B* **49**, 558 (1993).
38. G. Kresse, J. Hafner, Ab initio molecular-dynamics simulation of the liquid-metal–amorphous-semiconductor transition in germanium. *Phys. Rev. B* **49**, 14251 (1994).
39. P. E. Blöchl, Projector augmented-wave method. *Phys. Rev. B* **50**, 17953 (1994).
40. P. Larson, W. R. L. Lambrecht, Electronic structure and magnetism of europium chalcogenides in comparison with gadolinium nitride. *J. Phys.: Condens. Matter* **18**, 11333 (2006).
41. J. S. Smart, *Effective Field Theories of Magnetism* (W. B. Saunders Company, Philadelphia, 1966), pp. 76.
42. A. Jain *et al.*, The Materials Project: A materials genome approach to accelerating materials innovation. *APL Mater.* **1**, 011002 (2013).
43. B. Fultz, Vibrational thermodynamics of materials. *Prog. Mater. Sci.* **55**, 247 (2010).
44. G. Kresse, D. Joubert, From ultrasoft pseudopotentials to the projector augmented-wave method. *Phys. Rev. B* **59**, 1758 (1999).
45. A. Togo, I. Tanaka, First principles phonon calculations in materials science. *Scr. Mater.* **108**, 1 (2015).
46. Y. Wang *et al.*, Thermal equation of state of silicon carbide. *Appl. Phys. Lett.* **108**, 061906 (2016).

47. O. Hellman, I. A. Abrikosov, Temperature-dependent effective third-order interatomic force constants from first principles. *Phys. Rev. B: Condens. Matter Mater. Phys.* **88**, 144301 (2013).
48. O. Hellman, I. A. Abrikosov, S. I. Simak, Lattice dynamics of anharmonic solids from first principles. *Phys. Rev. B: Condens. Matter Mater. Phys.* **84**, 180301 (2011).
49. O. Hellman, P. Steneteg, I. A. Abrikosov, S. I. Simak, Temperature dependent effective potential method for accurate free energy calculations of solids. *Phys. Rev. B* **87**, 104111 (2013).
50. S. Nosé, A unified formulation of the constant temperature molecular dynamics methods. *Mol. Phys.* **52**, 255 (1984).
51. P. Giannozzi *et al.*, Advanced capabilities for materials modelling with Quantum ESPRESSO. *J. Phys.: Condens. Matter* **29**, 465901 (2017).
52. P. Giannozzi *et al.*, QUANTUM ESPRESSO: a modular and open-source software project for quantum simulations of materials. *J. Phys.: Condens. Matter* **21**, 395502 (2009).
53. O. Gunnarsson, Superconductivity in fullerides. *Rev. Mod. Phys.* **69**, 575 (1997).
54. H. Krakuer, W. E. Pickett, R. E. Cohen, Large calculated electron-phonon interactions in $La_{2-x}M_xCuO_4$. *Phys. Rev. B* **47**, 1002 (1993).
55. P. B. Allen, Neutron Spectroscopy of Superconductors. *Phys. Rev. B* **6**, 2577 (1972).
56. W. L. McMillan, Transition Temperature of Strong-Coupled Superconductors. *Phys. Rev. B* **167**, 331 (1968).
57. P. B. Allen, R. C. Dynes, Transition temperature of strong-coupled superconductors reanalyzed. *Phys. Rev. B* **12**, 905 (1975).
58. K. H. Bennemann, J. K. Garland, *Superconductivity in d- and f-band metals* (American Institute of Physics, New York, 1971).
59. O. V. Dolgov, I. I. Mazin, A. A. Golubov, S. Y. Savrasov, E. G. Maksimov, Critical Temperature and Enhanced Isotope Effect in the Presence of Paramagnons in Phonon-Mediated Superconductors. *Phys. Rev. Lett.* **95**, 257003 (2005).
60. M. J. Mehl, D. A. Papaconstantopoulos, Application of a New Tight-Binding Method for Transition Metals: Manganese. *Europhys. Lett.* **31**, 537 (1995).
61. M. M. Sigalas, D. A. Papaconstantopoulos, Calculations of the total energy, electron-phonon interaction, and Stoner parameter for metals. *Phys. Rev. B* **50**, 7255 (1994).
62. B. W. a. J. T. a. M. S. a. S. K. a. K. P. a. A. M. Oleś, Superconductivity of Mo_3Sb_7 from first principles. *Phys. Rev. B* **78**, 060507 (2008).
63. J. B. a. A. A. a. B. P. a. P. M. O. a. M. V. Milošević, Advanced first-principles theory of superconductivity including both lattice vibrations and spin fluctuations: The case of FeB_4. *Phys. Rev. B* **97**, 014503 (2018).
64. A. N. Christensen, The Temperature Factor Parameters of Some Transition Metal Carbides and Nitrides by Single Crystal X-Ray and Neutron Diffraction. *Acta Chem. Scand.* **32**, 89 (1978).
65. P. V. Villars, L. D. Calvert, *Pearson's Handbook of Crystallographic Data for Intermetllic Phases* (American Society for Metals, Metal Park, 1985).
66. E. J. Little, M. M. Jones, A complete table of electronegativities. *J. Chem. Educ.* **37**, 231 (1960).
67. E. I. Isaev, Phonon related properties of transition metals, their carbides, and nitrides: A first-principles study. *J. Appl. Phys.* **101**, 123519 (2007).
68. H. M. Tütüncü, S. Bağci, G. P. Srivastava, Electronic, elastic and phonon properties of the rock-salt LaSb and YSb. *J. Phys.: Condens. Matter* **19**, 156207 (2007).
69. S. H. Jhi, J. Ihm, S. G. Louie, M. L. Cohen, Electronic mechanism of hardness enhancement in transition-metal carbonitrides. *Nature* **399**, 132 (1999).
70. S. H. Jhi, S. G. Louie, M. L. Cohen, J. Ihm, Vacancy Hardening and Softening in Transition

Metal Carbides and Nitrides. *Phys. Rev. Lett.* **86**, 3348 (2001).
71. J. D. Budai *et al.*, Metallization of vanadium dioxide driven by large phonon entropy. *Nature* **515**, 535 (2014).
72. Z. Hiroi, Structural instability of the rutile compounds and its relevance to the metal–insulator transition of VO_2. *Prog. Solid State Ch.* **43**, 47 (2015).
73. G. Deinzer, G. Birner, D. Strauch, Ab initio calculation of the linewidth of various phonon modes in germanium and silicon. *Phys. Rev. B* **67**, 144304 (2003).
74. B. M. Klein, D. A. Papaconstantopoulos, Electron-phonon interaction and superconductivity in transition metals and transition-metal carbides. *Phys. Rev. Lett.* **32**, 1193 (1974).
75. W. Weber, Lattice Dynamics of Transition-Metal Carbides. *Phys. Rev. B* **8**, 5093 (1973).
76. H. R. Zeller, Effect of Lattice Instabilities on Superconducting and Other Properties in TaC_x. *Phys. Rev. B* **5**, 1813 (1972).
77. A. Furlan, U. Jansson, J. Lu, L. Hultman, M. Magnuson, Structure and bonding in amorphous iron carbide thin films. *J. Phys.: Condens. Matter* **27**, 045002 (2015).
78. A. Furlan, J. Lu, L. Hultman, U. Jansson, M. Magnuson, Crystallization characteristics and chemical bonding properties of nickel carbide thin film nanocomposites. *J. Phys.: Condens. Matter* **26**, 415501 (2014).
79. G. A. Landrum, R. Dronskowski, The Orbital Origins of Magnetism: From Atoms to Molecules to Ferromagnetic Alloys. *Angew. Chem. Int. Ed. Engl.* **39**, 1560 (2000).
80. J.-G. Cheng *et al.*, Pressure Induced Superconductivity on the border of Magnetic Order in MnP. *Phys. Rev. Lett.* **114**, 117001 (2015).
81. B. Roessli, P. Böni, W. E. Fischer, Y. Endoh, Chiral Fluctuations in MnSi above the Curie Temperature. *Phys. Rev. Lett.* **88**, 237204 (2002).
82. T. B. Coplen, Atomic Weights of the Elements. *J. Phys. Chem. Ref. Data* **26**, 1239 (1997).
83. J. Noffsinger, F. Giustino, S. G. Louie, M. L. Cohen, First-principles study of superconductivity and Fermi-surface nesting in ultrahard transition metal carbides. *Phys. Rev. B* **77**, 180507 (2008).
84. E. I. Isaev *et al.*, Phonon related properties of transition metals, their carbides, and nitrides: A first-principles study. *J. Appl. Phys.* **101**, 123519 (2007).
85. E. G. Maksimov, S. V. Ebert, M. V. Magnitskaya, A. E. Karakozov, Ab initio calculations of the physical properties of transition metal carbides and nitrides and possible routes to high-Tc. *J. Exp. Theor. Phys.* **105**, 642 (2007).
86. N. T. Huy *et al.*, Superconductivity on the Border of Weak Itinerant Ferromagnetism in UCoGe. *Phys. Rev. Lett.* **99**, 067006 (2007).
87. H. F. Yang *et al.*, Origin of the kink in the band dispersion of the ferromagnetic perovskite SrRuO3: Electron-phonon coupling. *Phys. Rev. B* **93**, 121102 (2016).
88. D. M. Edwards, Ferromagnetism and electron-phonon coupling in the manganites. *Adv. Phys.* **51**, 1259 (2002).
89. L. Ortenzi, S. Biermann, O. K. Andersen, I. I. Mazin, L. Boeri, Competition between Electron-Phonon coupling and Spin Fluctuations in superconducting hole-doped BiOCuS. *Phys. Rev. B* **83**, 100505 (2011).
90. D. Aoki, K. Ishida, J. Flouquet, Review of U-based Ferromagnetic Superconductors: Comparison between UGe2, URhGe, and UCoGe. *J. Phys. Soc. Jpn.* **88**, 022001 (2019).
91. D. E. Jackson *et al.*, Superconducting and magnetic phase diagram of $RbEuFe_4As_4$ and CsEuFe4As4 at high pressure. *Phys. Rev. B* **98**, 014518 (2018).
92. Y. Liu *et al.*, A new ferromagnetic superconductor: $CsEuFe_4As_4$. *Sci. Bull.* **61**, 1213 (2016).
93. D. Yi *et al.*, Tuning the competition between ferromagnetism and antiferromagnetism in a half-doped manganite through magnetoelectric coupling. *Phys. Rev. Lett.* **111**, 127601 (2013).

94. K. Balasubramanian, S. V. Khare, D. Gall, Energetics of point defects in rocksalt structure transition metal nitrides: Thermodynamic reasons for deviations from stoichiometry *Acta Materiala* **159**, 77 (2018).
95. Ohio-Supercomputer-Center, http://osc.edu/ark:/19495/f5s1ph73.

From systematic calculation and analysis of the thermodynamic and electronic properties of 3*d* transition metal carbides in the rocksalt structure, we identify MnC as a novel material displaying ferromagnetic superconductivity mediated by minority-spin-triplet Cooper pairs.